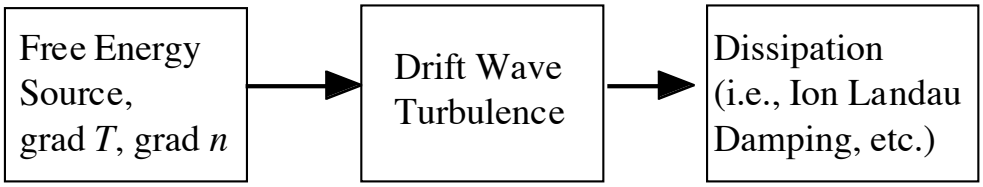

Classic Paradigm of Drift Wave Turbulence

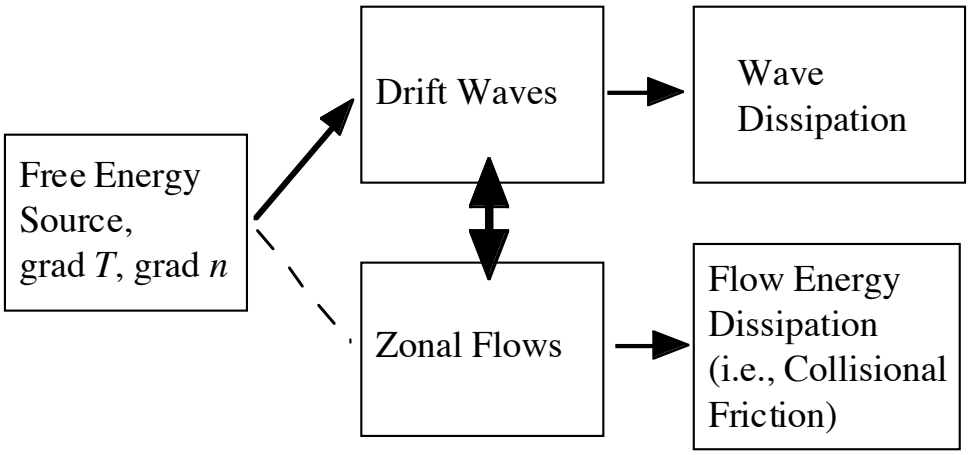

New Paradigm of Drift Wave-Zonal flow Turbulence

Fig. 1.1 New paradigm for the plasma turbulence.

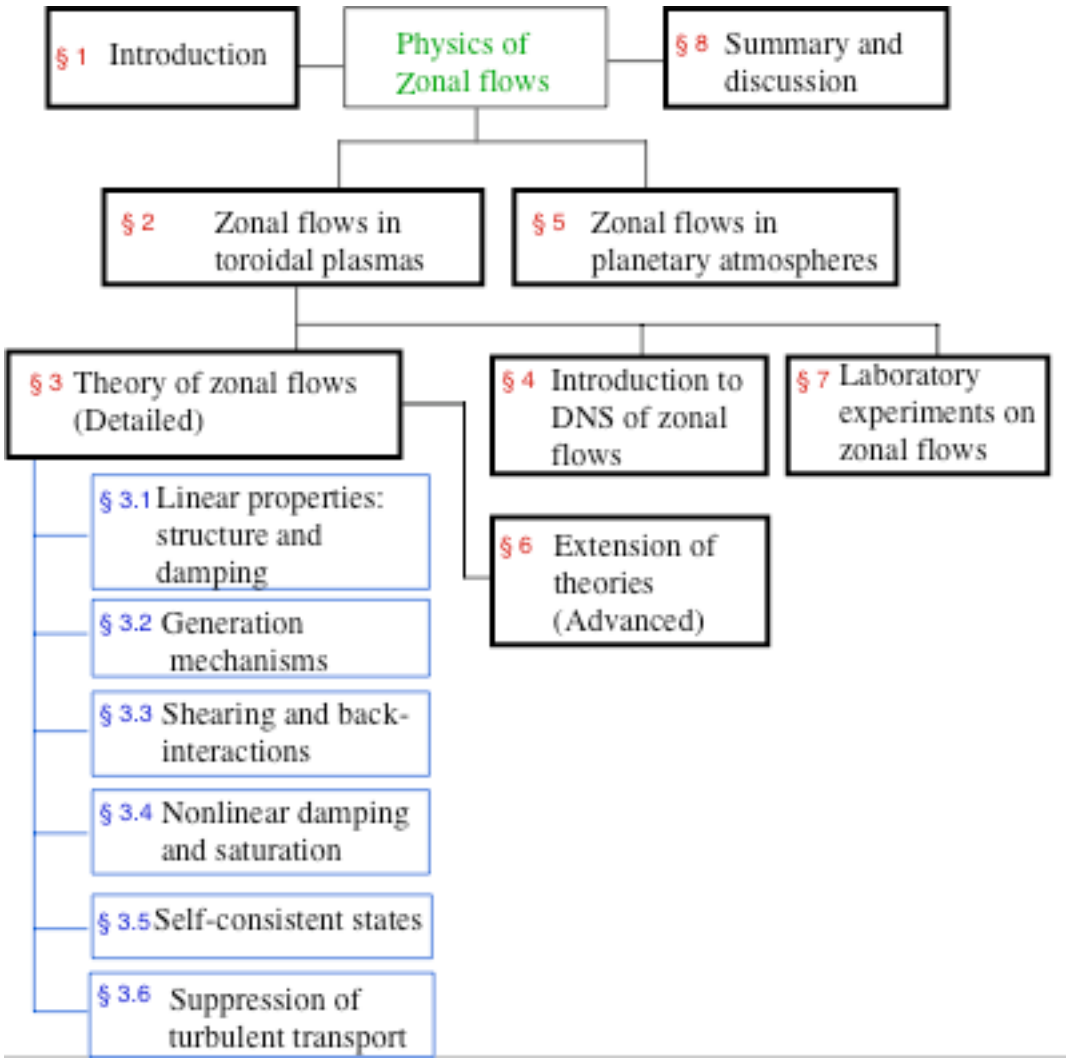

Fig.1.2 Road Map for the review.

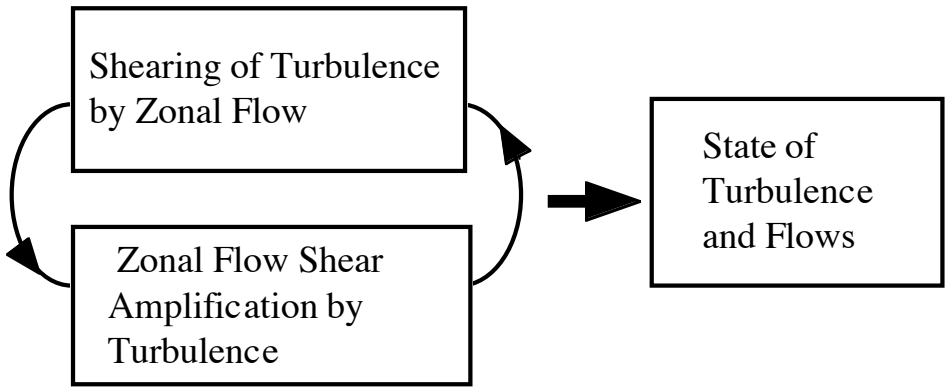

Fig.2.1 Mutual interaction of drift waves and zonal flows.

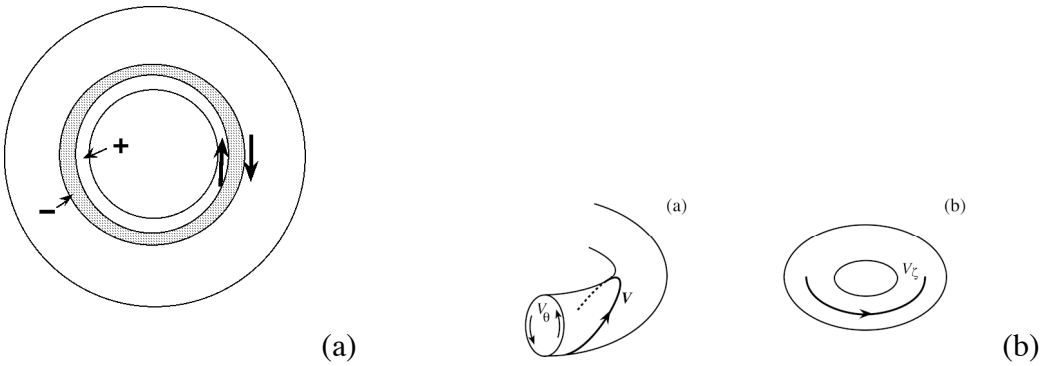

Fig.2.2. Zonal electric field and zonal flow. The poloidal crosssection of toroidal plasma is illustrated. Hached region and dotted region denote the positive and negative charges, respectively. (a) The flow perturbation in the poloidal cross-section. The bird-eye view of the net flow associated with the zonal perturbation is illustratrated in (b).

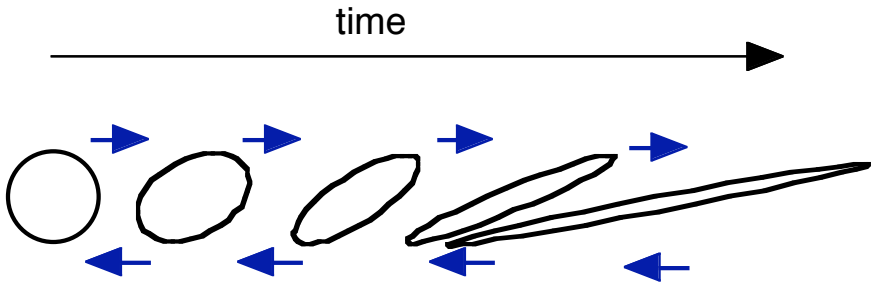

Fig.2.3 Shearing of the vortex.

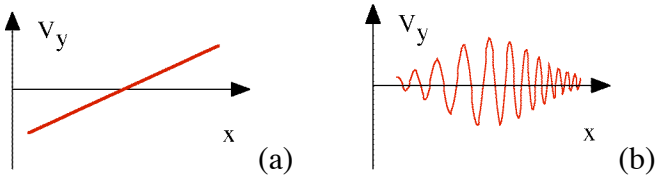

Fig.2.4 Sheared mean flow (a) and zonal flows (b) are illustrated.

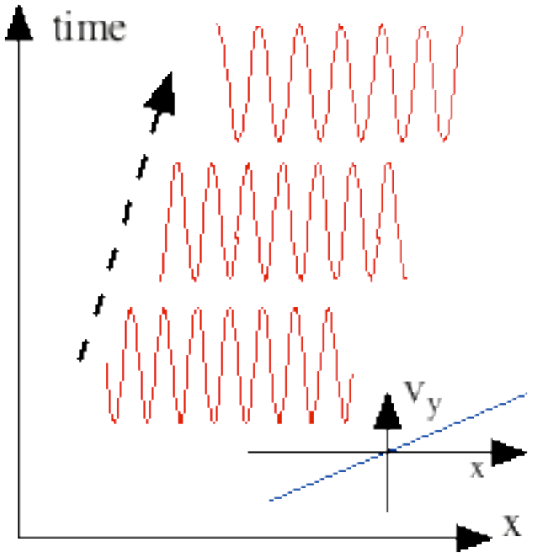

Fig.2.5 Drift wave in sheared flow field. When a drift wave packet is propagating in the x-direction in the presence of flow shear, $dV_y/dx > 0$, the wave number k_x changes.

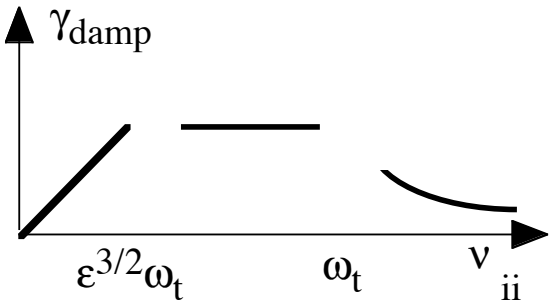

Fig. 3.1.1 Schematic drawing of the collisional damping rate for the zonal flow.

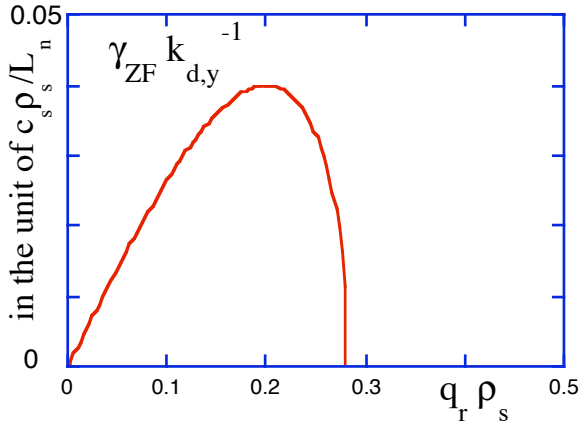

Fig.3.2.1 Growth rate of the zonal flow for the parametric modulational instability. A case of $e\tilde{\phi}_{d0}/T_e = 0.2\,\rho_s/L_n$ and $k_{d,x} = 0$ is shown.

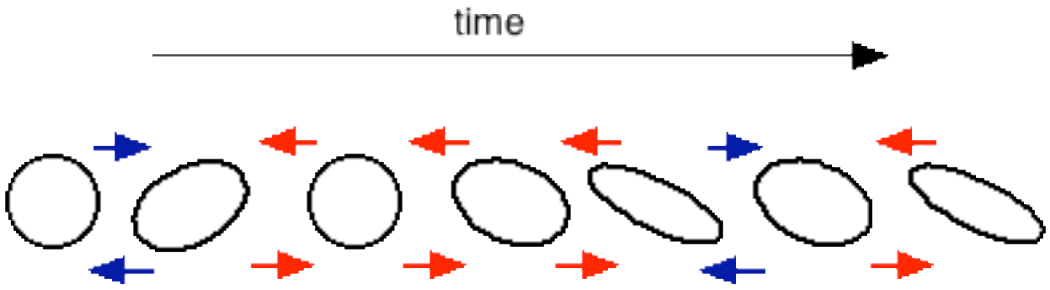

Fig.3.3.1 Random shearing flow and stretching. Shear flow (denoted by blue arrows or red arrows) is rapidly changing in time.

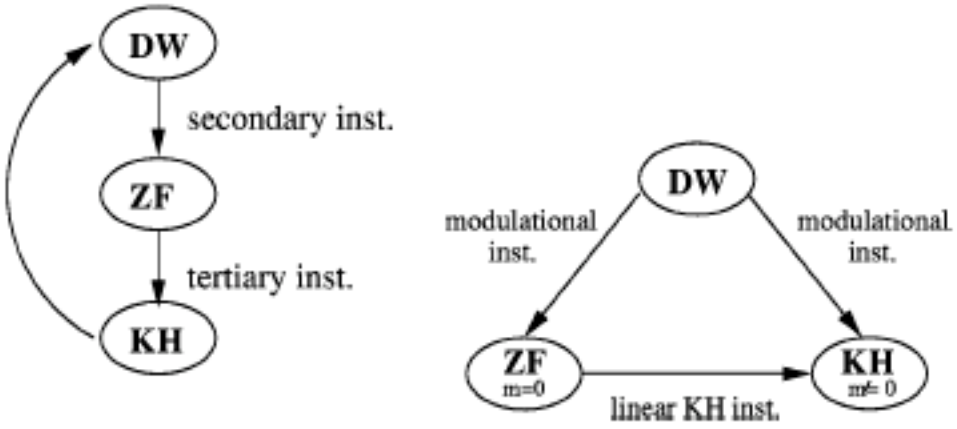

Fig. 3.4.1 The contrast of the linear view of the GKH modes (a) to a more general case where GKH modes are generated by both linear and nonlinear modulational instabilities (b). The linear view is hierarchical in that GKH is generated by the linear instability of zonal flows (ZF), which are already generated by DW. In general, GKH modes can, however, be generated directly from DW by modulational instability.

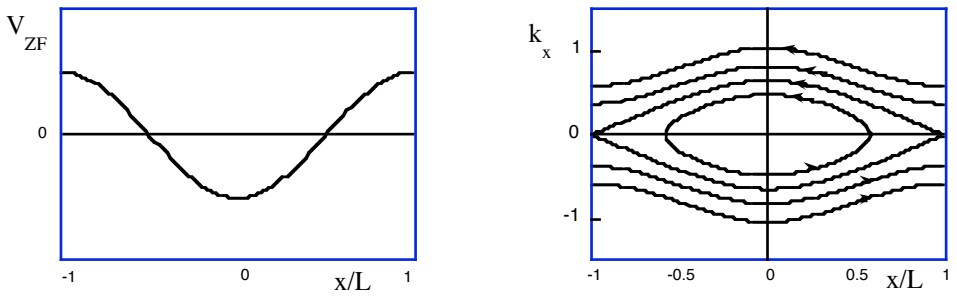

Fig.3.4.2 Trapping of wave-packets in the trough of zonal flow velocity. The spatial profile of zonal flow velocity (a) and trajectories in phase space (b).

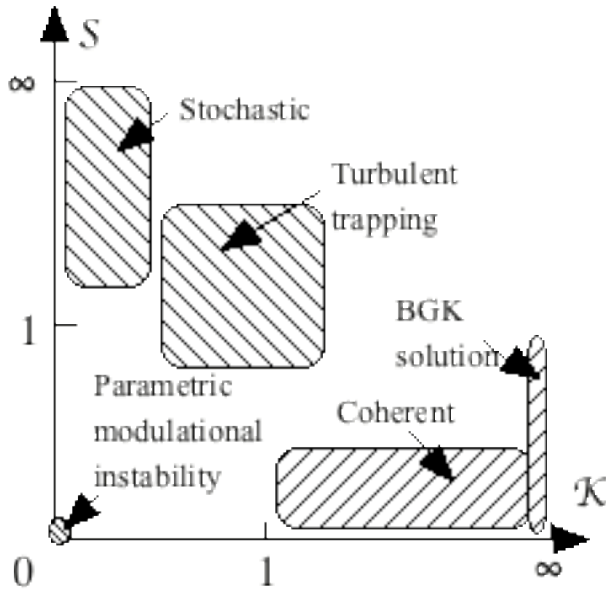

Fig.3.4.3 Parameter domains for various theoretical approaches.

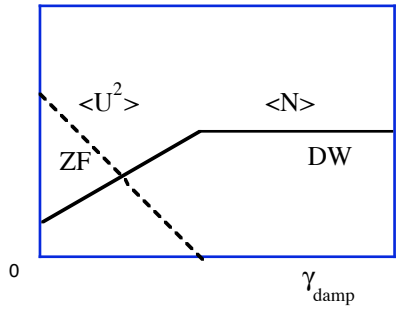

Fig.3.5.1 Amplitude of drift waves $\langle N \rangle$ and that of zonal flow $\langle U^2 \rangle$ for the case where the self-nonlinear stabilization effect of zonal flow (e.g., the $\gamma_{NL}\langle V^2 \rangle$ term in Eq.(2.10b)) exists. It shows the γ_{damp}-dependence with fixed γ_L.

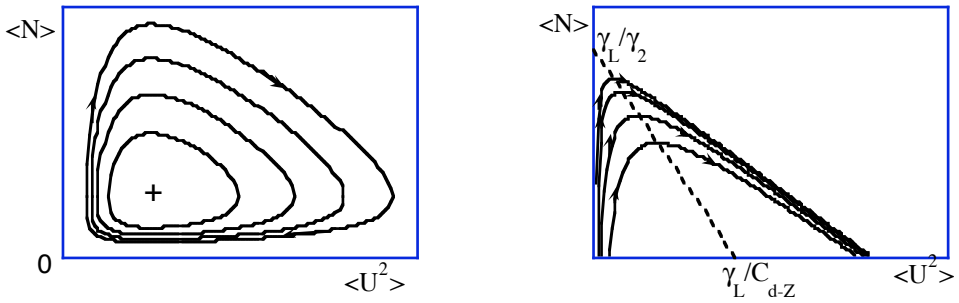

Fig.3.5.2 Phase portrait in the absence of nonlinear stabilization effect of drift waves, $\gamma_2 = 0$, [2.14] (a). Trajectory in the case of no zonal flow damping $\gamma_{damp} = 0$ is shown in (b). Depending on the initial conditions, the system reaches different final states, in which the waves are quenched.

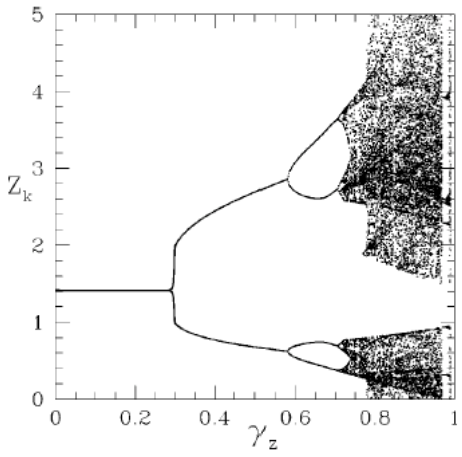

Fig.3.5.3 Normalized amplitude of zonal flow Z_k as a function of the normalized damping rate $\gamma_z = \gamma_{damp}/\gamma_L$. Quoted from [2.23].

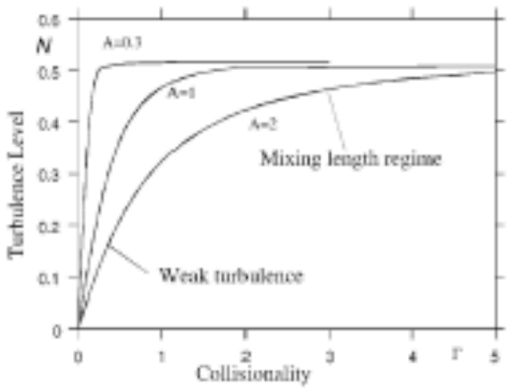

Fig.3.5.4 Amplitude of drift waves (normalized to $2\gamma_L/\gamma_2$) in the stationary state as a function of the collisional damping rate of zonal flow γ_{damp} . The horizontal axis is taken γ_{damp}/γ_L in the unstable region $|k_r| < k_{rc}$. In this figure, A is a parameter that is in proportion to $C_{d\to Z}/\gamma_2$. (quoted from [3.44].)

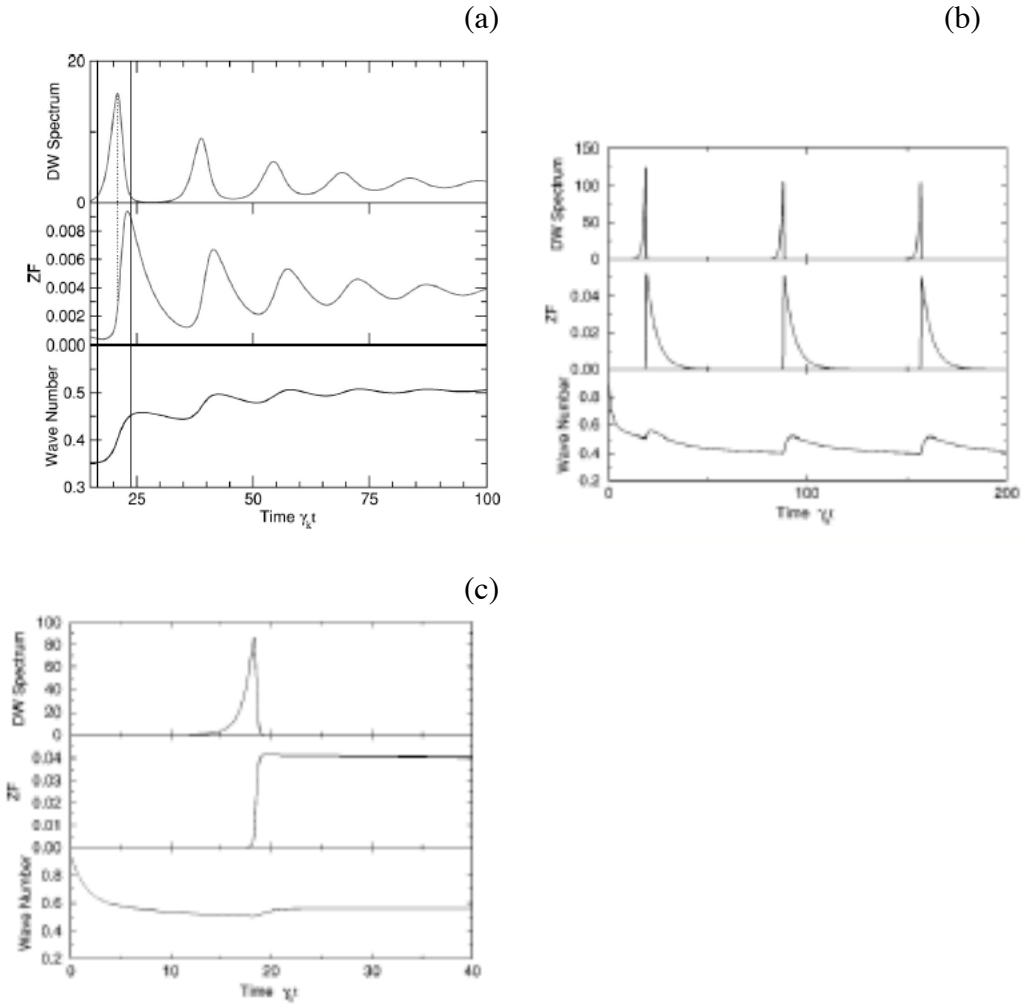

Fig.3.5.5 Temporal evolution of drift wave energy, zonal flow and the average wave number. cases of $\gamma_L \neq 0$, $\gamma_{damp} \neq 0$, $\gamma_2 \neq 0$ (a), $\gamma_2 = 0$ (b) and $\gamma_{damp}=0$ (c) are shown. [3.92].

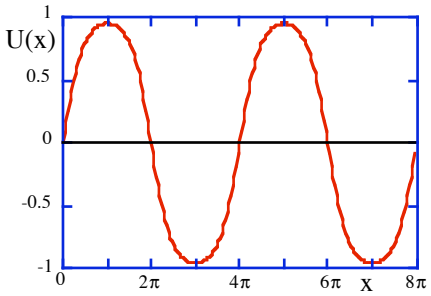

Fig.3.5.6 Coherent profile of normalized zonal flow vorticity.

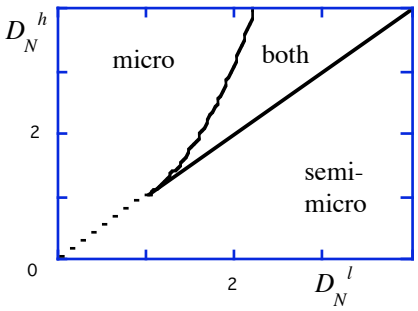

Fig.3.5.7 Phase diagram for the case of mutual interactions between intermediate scale and micro modes.

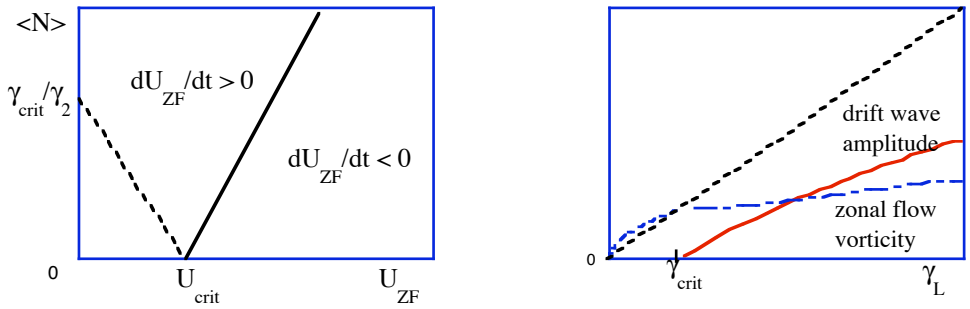

Fig.3.5.8 Marginal stability boundary for the growth of the zonal flow is shown by the solid line in the limit of $\gamma_{damp} = 0$ (a). Dotted line indicates the marginal stability condition for the drift waves (a). The excited energy of waves and flows as a function of the growth rate of drift waves, in the limit of $\gamma_{damp} = 0$ (b).

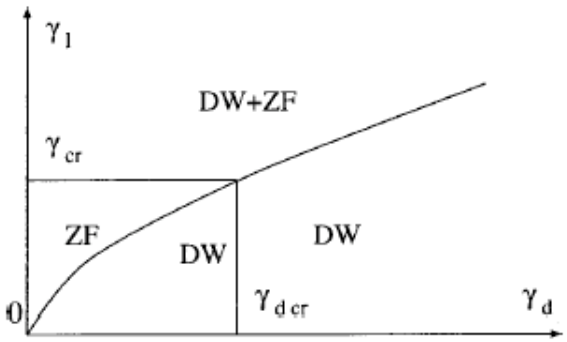

Fig.3.5.9 The diagram, indicating the regions of residual drift wave, and zonal flow turbulence as well as the region where they coexist in the $\left(\gamma_L, \gamma_{\text{damp}}\right)$ plane.

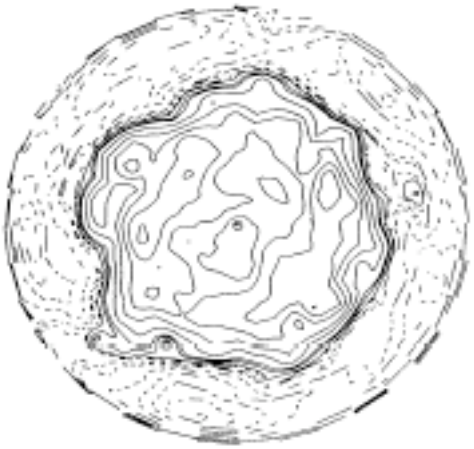

Fig.4.1 Contour of electrostatic potential from the simulation of [2.6].

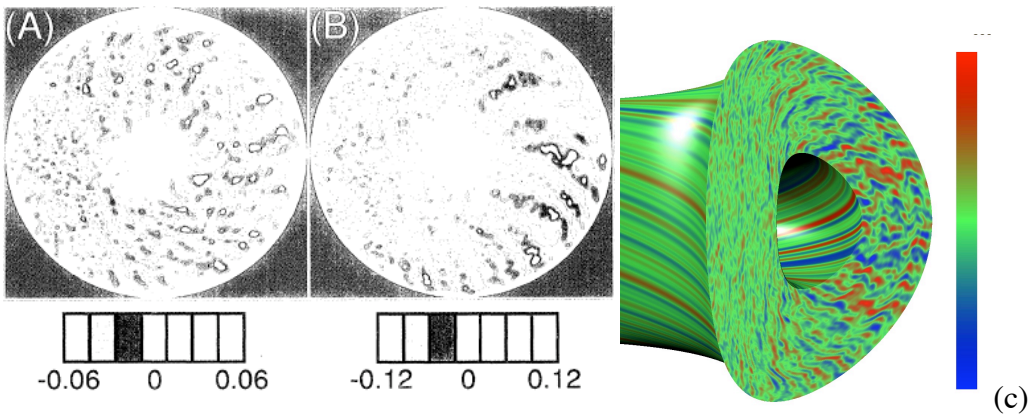

Fig. 4.3 Radial size of turbulent eddies shown in colored contour of ambient density fluctuation gets reduced due to the random shearing by self-generated $\boldsymbol{E}\times\boldsymbol{B}$ zonal flows from gyrokinetic particle simulation, (a) and (b) (from [2.16]). (c) is quoted from http://fusion.gat.com/comp/parallel/gyro_gallery.html.

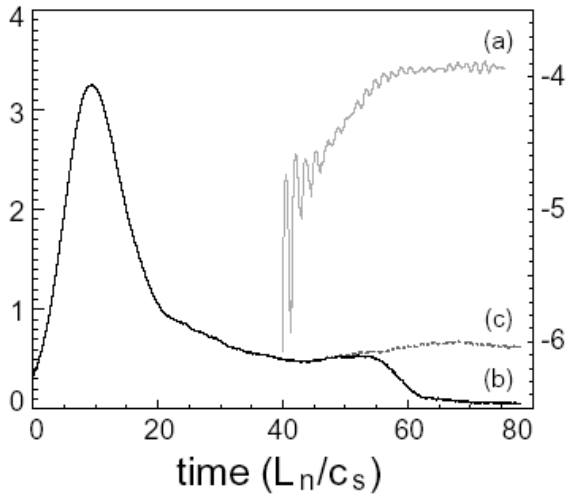

Fig.4.3. Temporal evolution of the amplitude of the zonal flow, on log scale (a), and turbulence level (b) and (c) on linear scale [2.13].

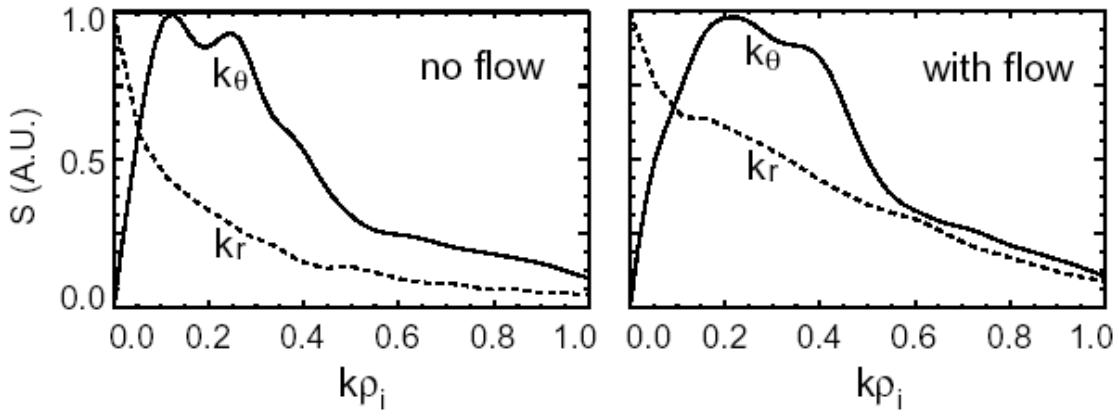

Fig.4.4 k_r spectrum of the ambient density fluctuation from gyrokinetic particle simulation is broadened due to random shearing of eddies by self-generated $\boldsymbol{E}\times\boldsymbol{B}$ flows (dashed lines) [3.77]

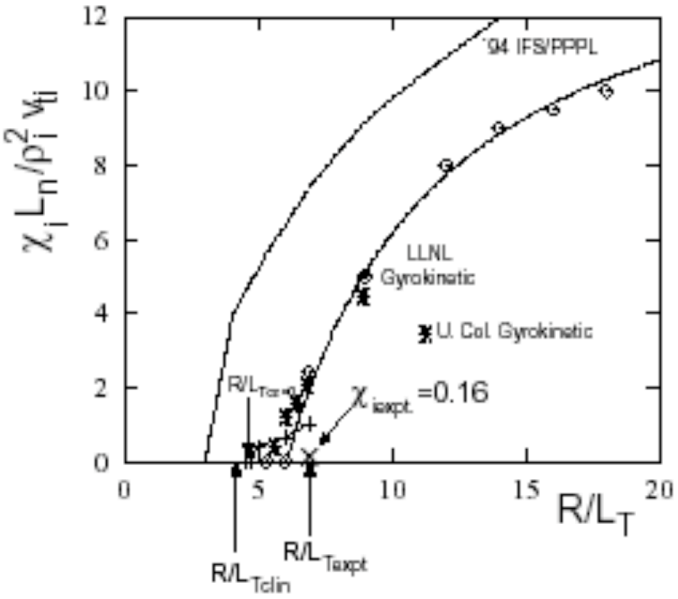

Fig.4.5 Dependence of ion thermal conductivity by ITG turbulence on the ion temperature gradient (collisionless limit). from [4.15]

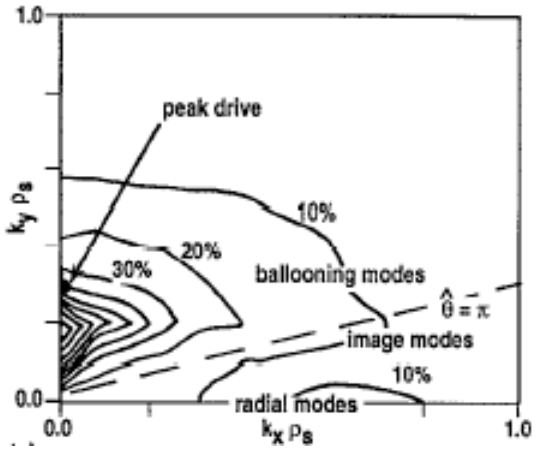

Fig. 4.6 Contour of fluctuation spectrum from [2.17].

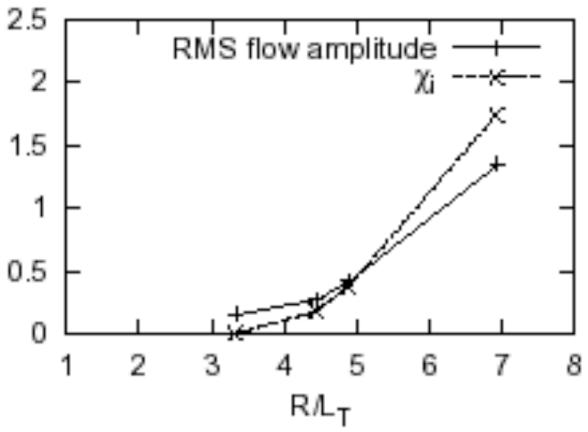

Fig.4.7 Dependence of the turbulence level (shown by ion thermal conductivity) and zonal flow amplitude on the ion temperature gradient. (from [4.16])

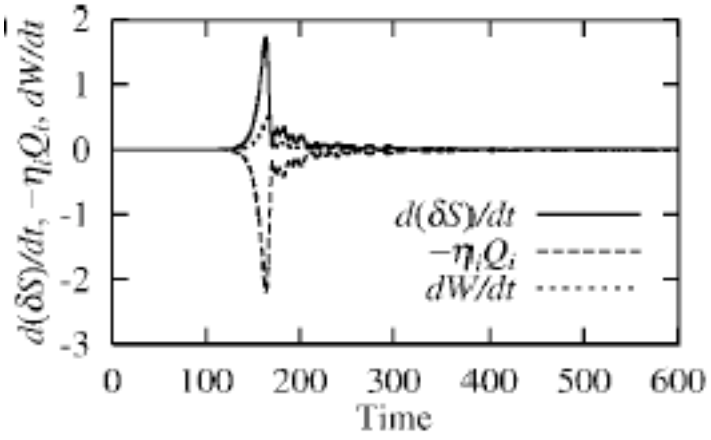

Fig.4.8 Transient burst of ITG turbulence and associated transport in the collisionless limit. [3.109]

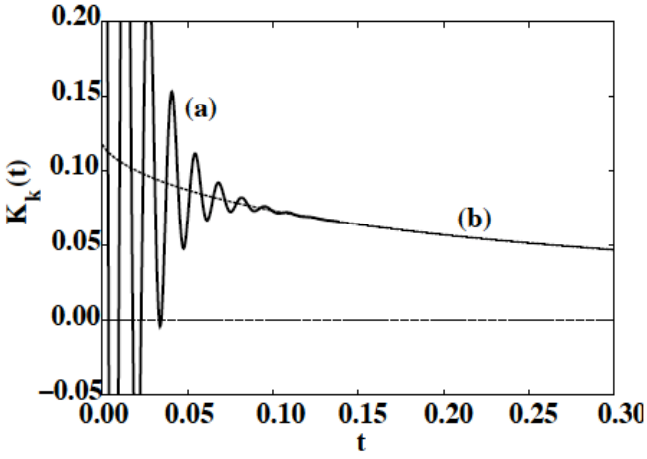

Fig.4.9 Transient evolution of the poloidal flow and approach to the R-H zonal flow. $K(t) = \phi(t)/\phi(0)$ is the normalized potential and time is normalized to τ_{ii} . (from [2.37])

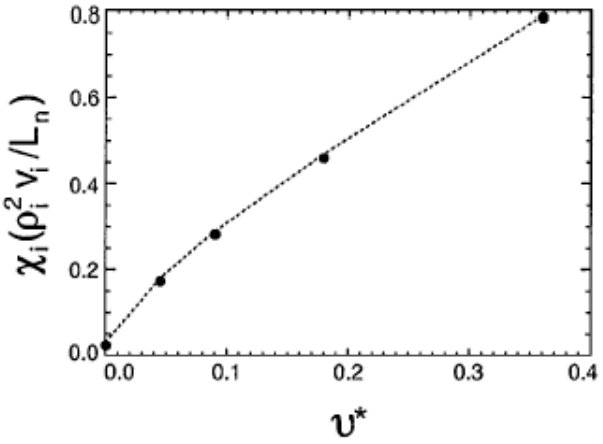

Fig. 4.10 Ion heat conductivity in nonlinear gyrokinetic simulations with $R/L_T = 5.3$ vs the ion-ion collision frequency [2.49].

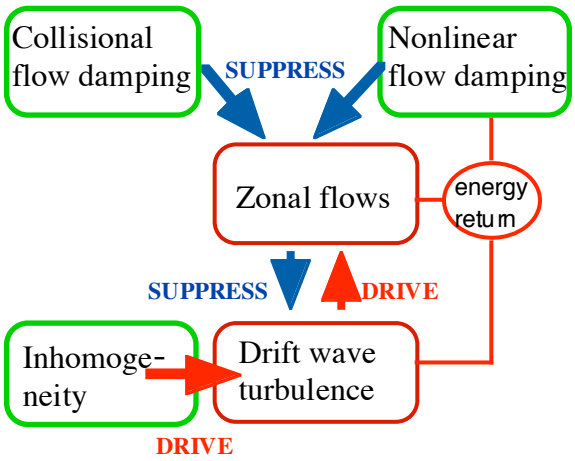

Fig. 4.11 Schematic illustration of the self-regulation. In the right circle, 'energy return' indicates the process of energy return to drift waves (being investigated.)

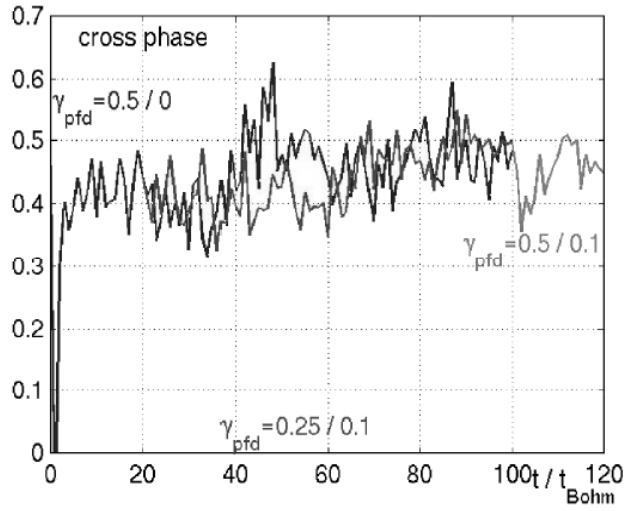

Fig. 4.12 Cross phase evaluated at the radial position where the ZFs are persistently localized ($r/a = 0.8$) for all the simulations with $\rho_* = 0.02$ versus time. γ_{pfd}, the poloidal damping rate normalized to c_s/qR, is varied as indicated. [4.19].

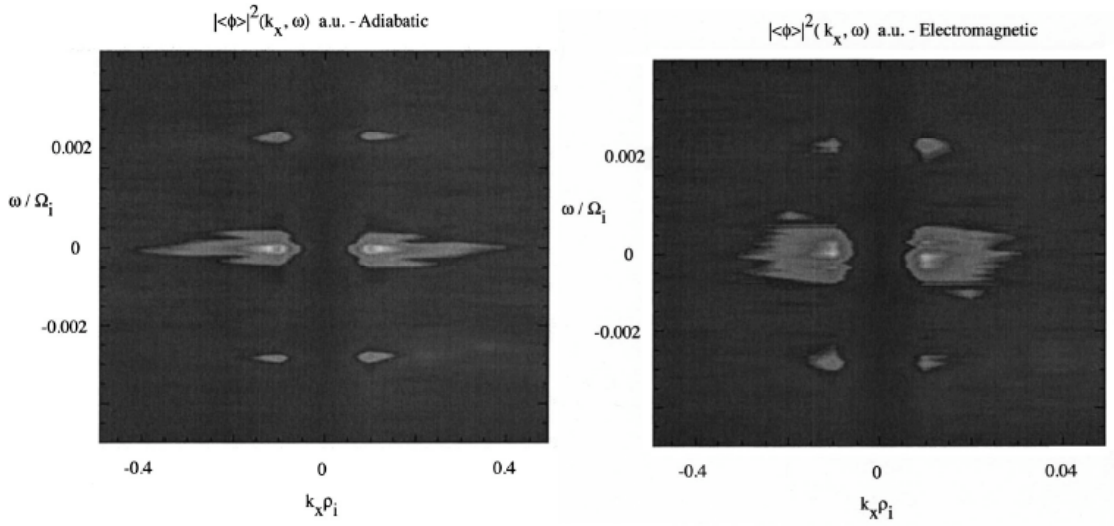

Fig.4.13 Frequency spectrum of the zonal flows in collisionless trapped electron mode (CTEM) turbulence. Note a peak of pure zonal flow near $\omega = 0$ and that at GAO frequency $\omega_{\text{GAO}} = v_{\text{Thi}}/R$. The influence of non-adiabatic response of electrons is illustrated. The case without (left) and with (right) are shown. In the presence of nonadiabatic response of electrons, the power spectrum of zonal flow component becomes wider. [4.23]

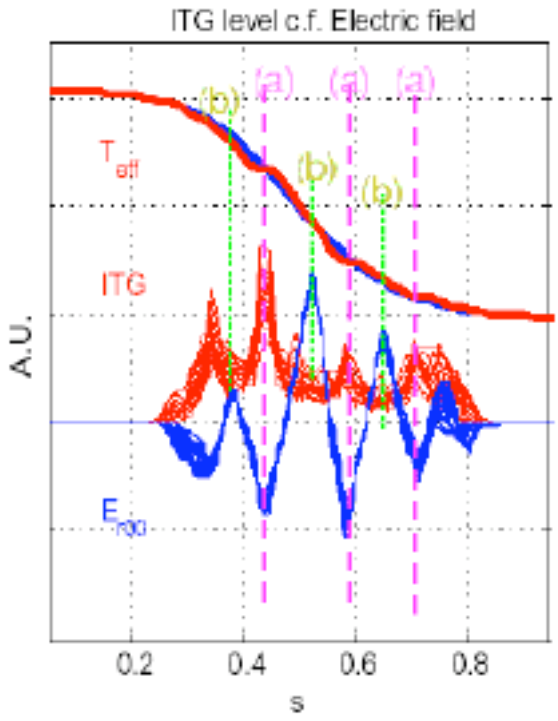

Fig.4.14 Snapshots of the zonal $\boldsymbol{E}\times\boldsymbol{B}$ flow, ITG amplitude, and effective temperature profile in the nonlinear stage. [4.26]

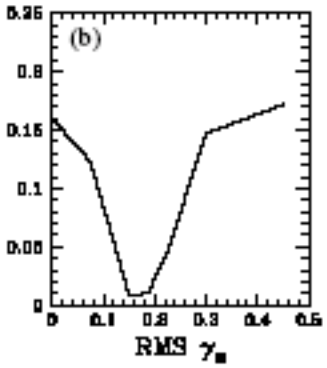

Fig.4.15 Growth rate of tertiary instability [2.51]

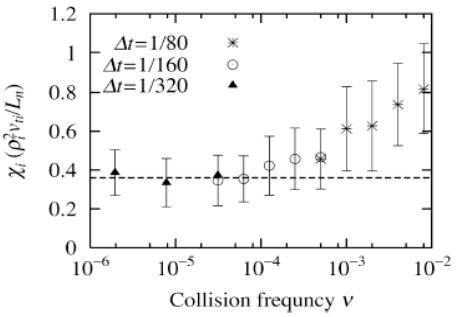

Fig.4.16 Asymptotic convergence of the turbulent transport in the collisionless limit. from [4.33]

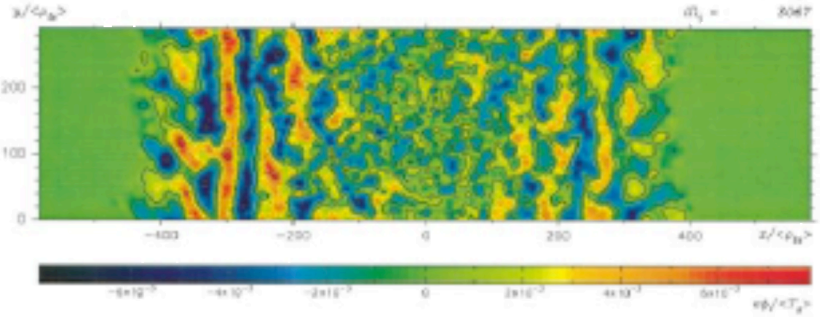

Fig.4.17 Two dimensional contour of the electrostatic potential perturbation of ETG turbulence near the q-minimum surface $x = 0$.[2.52]

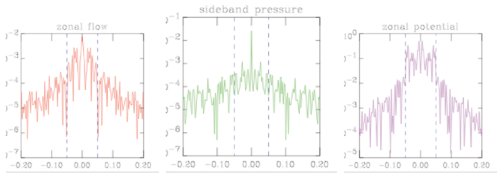

Fig. 4.18 Frequency spectrum of the zonal flows from gyrofluid simulation of edge drift-Alfven turbulence [4.66]. Note a significant intensity spectrum from zero frequency all the way up to the GAO frequency ω_{GAO} , without a distinct single peak.

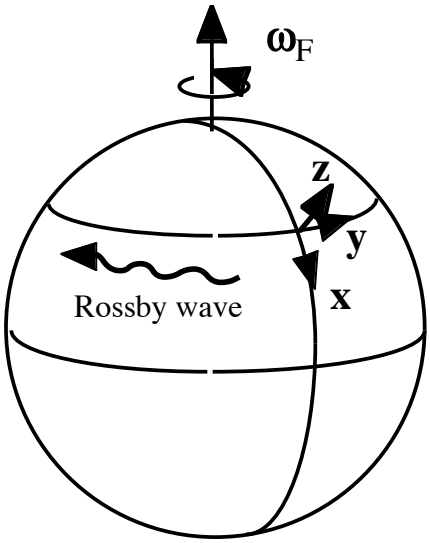

Fig. 5.1.2 Rotating sphere. Coordinates on a rotating sphere are: The x-axis in the direction of latitude (from pole to equator), y-axis in the direction of longitude, and z-axis in the vertical direction. Propagation of Rossby wave in the westward direction.

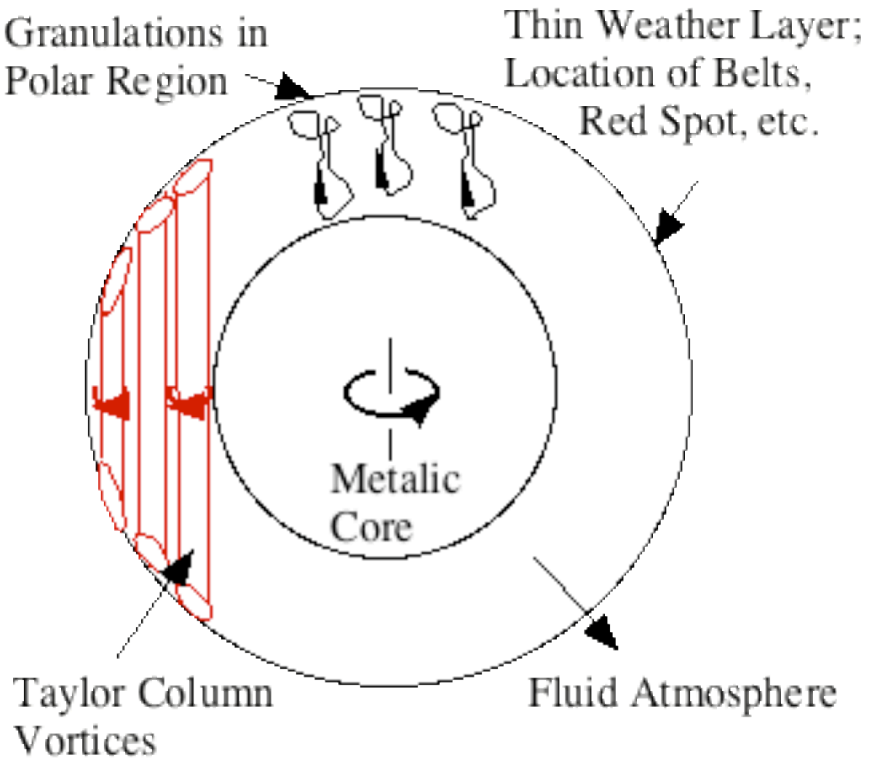

Fig.5.2.1 Schematic drawing of convection phenomena in Jovian atmosphere. Schematic depiction of zonal belt formation in secondary bifurcation scenario is also shown. Northern and southern projections of Taylor column onto Weather Layer with tilting modulation and bifurcation.

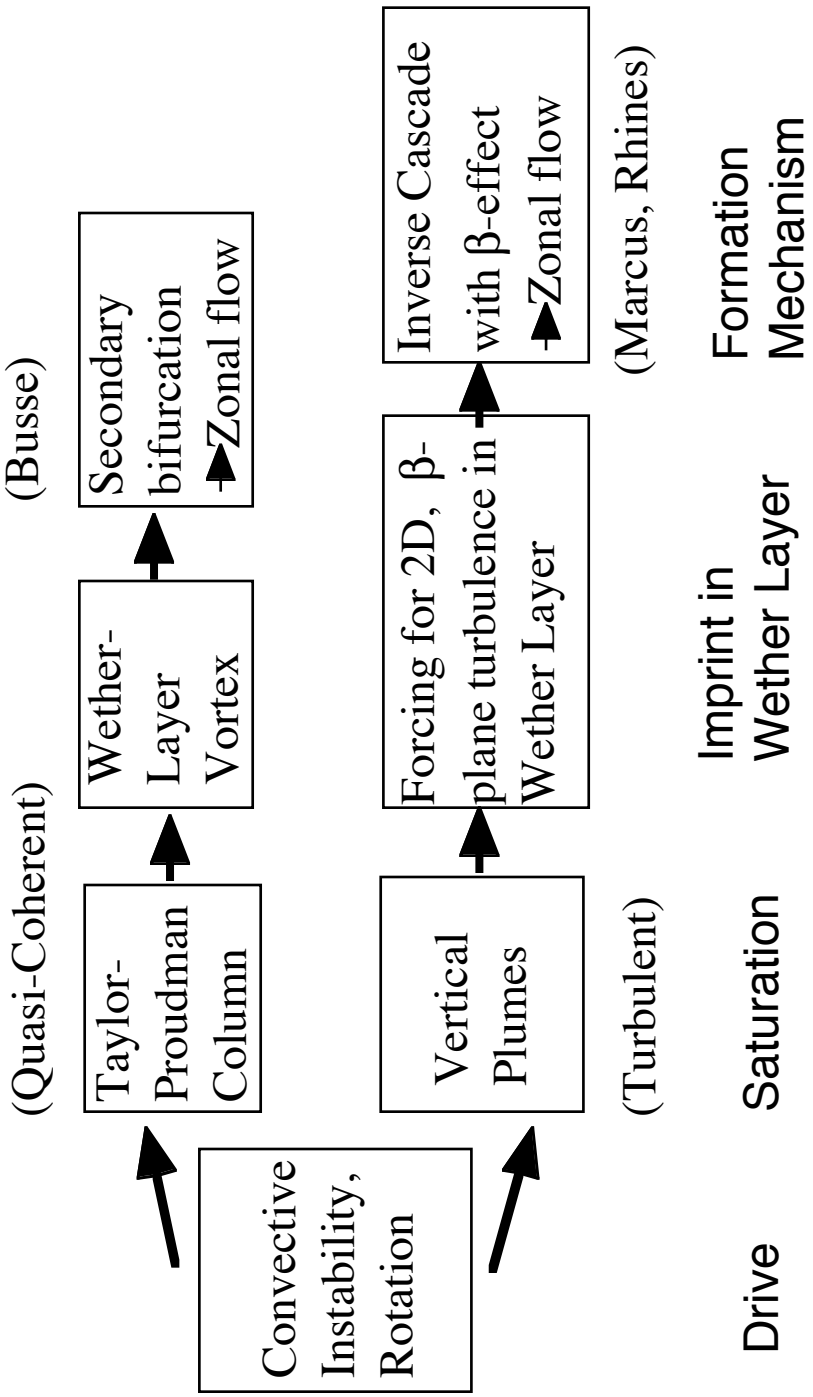

Fig.5.2.2 The assumptions and logic of the two scenarios.

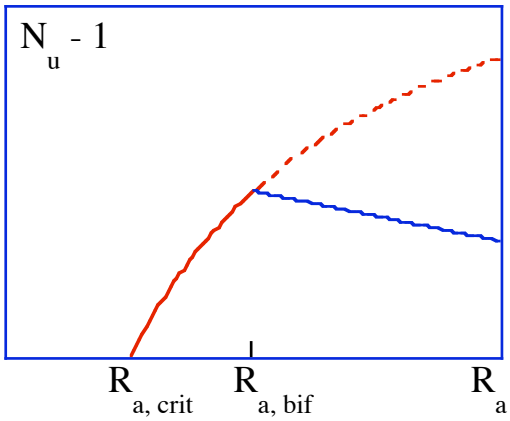

Fig.5.2.3 Cartoon of secondary bifurcation scenario [5.4].

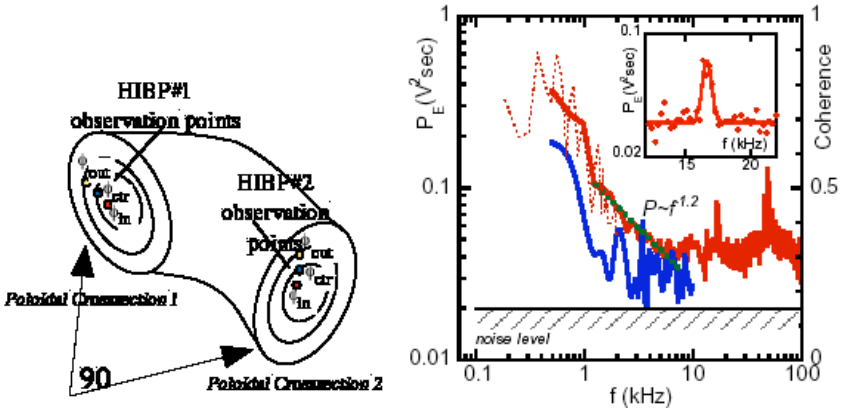

Fig.7.1 Identification of zonal flow on CHS. Geometry of measurements and fluctuation spectra. (a) Observation points of dual heavy ion beam probes in CHS. (b) Power spectra of a electric field, and coherence between electric fields from the HIBPs. In the frequency range from 0.3 kHz to 1 kHz, the activity to show long range correlation is found to be zonal flow. A peak at the GAM frequency is shown by an insert. Fluctuations in the range of tens of kHz are drift-wave turbulence. [7.17]

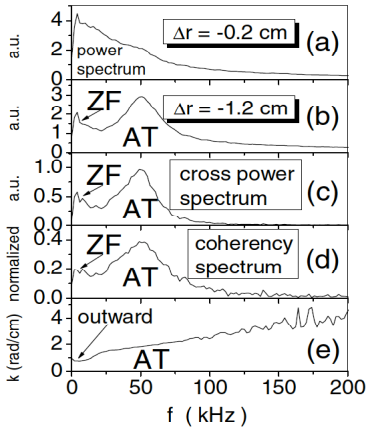

Fig. 7.2 Spectra measured with the modified forked probe. Peaks of zonal flow and ambient turbulence (AT) are shown. (a) Auto power spectrum of $\tilde{V}_{\theta 1}$ ($\Delta r = -0.2$ cm). (b) Auto power spectrum of $\tilde{V}_{\theta 2}$ ($\Delta r = -1.2$ cm). (c) Cross power spectrum. (d) Coherency spectrum. (e) Wave number spectrum. (c), (d). and (e) were calculated from the long distance correlation between $\tilde{V}_{\theta 1}$ and $\tilde{V}_{\theta 2}$. [7.19]

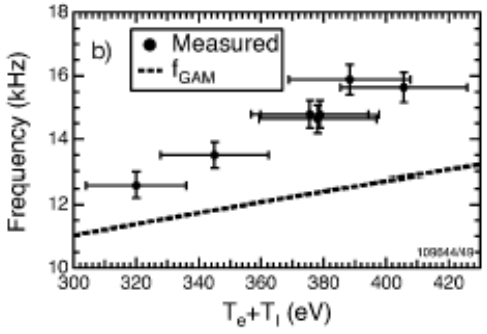

Fig.7.3 Frequency of observed oscillations (attributed to GAM) and it dependence on temperature. Measurement of D III-D is compared to the calculated GAM frequency (left) [7.37].